Paleoceanography and Paleoclimatology

RESEARCH ARTICLE
10.1029/2019PA003656

Hydrologic Change in New Zealand During the Last Deglaciation Linked to Reorganization of the Southern Hemisphere Westerly Winds

Jessica L. Hinojosa[1,2], Christopher M. Moy[3], Marcus Vandergoes[4], Sarah J. Feakins[5], and Alex L. Sessions[1]

[1]Division of Geological and Planetary Sciences, California Institute of Technology, Pasadena, CA, USA, [2]Now at Shell International Production and Exploration, Houston, TX, USA, [3]Department of Geology, University of Otago, Dunedin, New Zealand, [4]Department of Paleontology and Environmental Change, GNS Science, Lower Hutt, New Zealand, [5]Department of Earth Sciences, University of Southern California, Los Angeles, CA, USA

Key Points:
- We use a multiproxy approach to reconstruct lake balance and isotopic signature at Lake Hayes, New Zealand, during the last deglaciation
- We present evidence for a wetter Antarctic Cold Reversal and drier Younger Dryas and early Holocene in southern New Zealand
- We link these climate anomalies to migrations of the Southern Hemisphere westerly winds

Supporting Information:
- Data S1. Supporting Information

Correspondence to:
J. L. Hinojosa,
jess.l.hinojosa@gmail.com

Citation:
Hinojosa, J. L., Moy, C. M., Vandergoes, M., Feakins, S. J., & Sessions, A. L. (2019). Hydrologic change in New Zealand during the last deglaciation linked to reorganization of the Southern Hemisphere westerly winds. *Paleoceanography and Paleoclimatology*, *34*, 2158–2170. https://doi.org/10.1029/2019PA003656

Received 13 MAY 2019
Accepted 8 NOV 2019
Accepted article online 13 NOV 2019
Published online 26 DEC 2019

Abstract Millennial-scale climate anomalies punctuating the last deglaciation were expressed differently in the Northern and Southern Hemispheres. While changes in oceanic meridional overturning circulation have been invoked to explain these disparities, the nearly synchronous onset of such events requires atmospheric mediation. Yet the extent and structure of atmospheric reorganization on millennial timescales remains unclear. In particular, the role of the Southern Hemisphere westerly winds and associated storm tracks is poorly constrained, largely due to the paucity of accessible archives of wind behavior. Here we present a new paleohydrologic record from a Lake Hayes, New Zealand (45°S), sediment core from ~17–9 ka. Using two independent proxies for lake hydrology (Ca/Ti in sediments and δD values of aquatic plant biomarkers), we find evidence for a wetter Antarctic Cold Reversal (14.7–13.0 ka) and a drying trend during the Younger Dryas (12.9–11.6 ka) and early Holocene (11.7 ka onward in this record). Comparisons of the Lake Hayes record with other Southern Hemisphere sites indicate coherent atmospheric shifts during the Antarctic Cold Reversal and Younger Dryas, whereby the former is wetter/cooler and the latter is drier/warmer. The wet/cool phase is associated with a northward shift and/or strengthening of the Southern Hemisphere westerly winds, whereas the drier/warmer phase indicates weaker midlatitude winds. These climatic trends are opposite to the Northern Hemisphere. There is a decoupling of climatic trends between Southern Hemisphere low-latitude and midlatitude climates in the early Holocene, which could be explained by several mechanisms, such as the retreat of Antarctic sea ice.

Plain Language Summary In this study, we reconstruct climate in New Zealand at the end of the last glacial period. We do this by measuring "proxies" of ancient climate from ~17,000 to 9,000 years ago stored in lake sediments from Lake Hayes, New Zealand. Our findings suggest there were 1,000-year swings in climate, going between wetter and drier conditions at Lake Hayes. These trends are seen in other Southern Hemisphere locations and match similar climate intervals around the world. We interpret the climate shifts to be related to north-south movement of the Southern Hemisphere westerly winds, an important but understudied part of the global climate system.

1. Introduction

During the last deglaciation, middle to high latitudes (>40°) of each hemisphere experienced millennial-scale climate anomalies of opposing temperature and moisture balance (summarized in Denton et al., 2010). Much emphasis has been placed on oceanic meridional overturning as an explanation for these opposing climate patterns (e.g.,Barker et al., 2009 ; Broecker, 1998 ; Clark et al., 2002), whereby changes in the strength and geometry of thermohaline circulation altered the redistribution of heat globally. However, near-synchronous climate shifts in both hemispheres cannot be caused or forced exclusively by oceanic transport due to the ocean mixing time of ~1 kyr, implicating atmospheric transfer of heat and energy as well (e.g.,Chase et al., 2015 ; Pedro et al., 2016 ; Wunsch, 2006).

If the atmosphere played a significant role in these climate anomalies, changing wind strength and precipitation patterns should be evident in climate archives. Of particular focus are the Northern Hemisphere (NH) Bølling-Allerød (BA) interstadial (~14.8–13.0 ka), coincident with the Southern Hemisphere (SH) Antarctic

Cold Reversal (ACR), and the Younger Dryas (YD) stadial in the NH coincident with high-latitude warming in the SH (e.g.,Brauer et al., 2008 ; Hodell et al., 2012 ; Liu et al., 2013). During both of these intervals, the NH and SH, respectively, experienced opposite temperature anomalies, with a warm NH/cool SH during the BA/ACR followed by a reversal during the YD (Clark et al., 2012; Denton et al., 2010). Temperature has been a primary focus of midlatitude and high-latitude paleoclimate studies, but there remains a poor understanding of past hydrologic change in the SH. Importantly, there are few records from the midlatitudes, which are dominated by the

Hemisphere westerly winds (SHWW) and associated storm tracks, that can directly evaluate changes in hydrologic balance associated with westerly derived precipitation. Migrations of the SHWW affect regulation of atmospheric CO_2 (Anderson & Carr, 2010; Toggweiler et al., 2006), pace of oceanic circulation (Klinger & Cruz, 2009), and SH climate (Garreaud et al., 2013). Thus, understanding controls on and records of past SHWW behavior is critical for regional as well as global climate.

Here we present a new paleohydrologic reconstruction from a lake sediment core collected in southwest New Zealand that spans the Late Glacial-early Holocene transition. We combine records of endogenic Ca enrichment (Ca/Ti) and aquatic and terrestrial plant *n*-alkane hydrogen isotope ratios (δD_{C23} and $\delta D_{long\text{-}chain}$) to identify intervals of regional moisture shifts associated with the strength and latitudinal position of the SHWW and associated storm tracks. We compare our proxy data with records from the SH midlatitudes, spanning multiple ocean basins, latitudes, and archive types, as well as zonal winds extracted from the TraCE-21 ka coupled atmosphere-ocean general circulation model (He, 2011).

2. Regional Setting and Proxy Justification

2.1. Lake Hayes, New Zealand

Lake Hayes (44.98°S, 168.81°E) is a small holomictic lake located on New Zealand's South Island. The lake has a maximum depth of 33 m, surface area of 2.76 km^2, and catchment area of 44 km^2 and at present has a single inlet and outlet (Figure 1). Today, strong thermal stratification and the addition of excess macronutrients from the surrounding developed and agricultural catchment leads to hypolimnetic anoxia during most summers (Otago Regional Council, 2009). The combination of a single outlet, shallow lake bathymetry, and location in semiarid Central Otago east of the main topographic divide make Lake Hayes sensitive to past changes in hydrology. West of the divide, mean annual precipitation can exceed 6 m/yr (Salinger & Mullan, 2001), but at Lake Hayes mean annual rainfall averages 0.7 m/yr (extracted from the National Institute of Water and Atmospheric Research CliFlo database at cliflo.niwa.co.nz). Twenty-four-hour Penman potential evapotranspiration was measured from 2007–2010 at a nearby weather station in Queenstown, New Zealand (NIWA CliFlo station ID: 48), yielding an average of 2.2 $\pm$ 1.6 mm (Frew, 2015).

Low-pressure systems form over the Southern Ocean, and storms are moved via eddy transport toward the South Island by the strongest westerly winds. The Southern Alps form an orographic barrier to this moisture, with Lake Hayes in the rain shadow. Thus, most precipitation that reaches Lake Hayes arrives from the south and southwest as atmospheric eddies that spin northward from the core of the westerly wind belt (Figure 2). The primary moisture source for this precipitation is the Southern Ocean (Purdie et al., 2010) (Figure 2). Though there is limited precipitation seasonality (Figure 2), high-volume storm events are more frequent in the winter, when the SHWW are shifted farthest north. This suggests a modern link between SHWW shifts and moisture delivery to Lake Hayes. We hypothesize that longer-term northward shifts and/or intensification of the storm tracks would similarly result in wetter conditions at Lake Hayes. Conversely, we would expect drier conditions when the storm tracks shifted farther south or weakened. There is evidence for this relationship during the twentieth century, where anomalously wet years on the South Island are associated with anomalously strong westerly winds (Ummenhofer & England, 2007).

2.2. Isotopic Mass Balance in Lake Hayes

Lake water hydrogen isotopic composition (δD_{lake}) is influenced by hydrologic balance, as increased evaporation or reduced input would lead to isotopic enrichment of the heavy isotopes (^2H and ^{18}O) (Gat, 1996). δD_{lake} may also be altered by precipitation isotopic composition changes associated with storm track shifts, as precipitation from higher latitudes would be D-depleted relative to that from lower latitudes (IAEA/WMO, 2016). At Lake Hayes, because most precipitation comes from the south (Figure 2), both

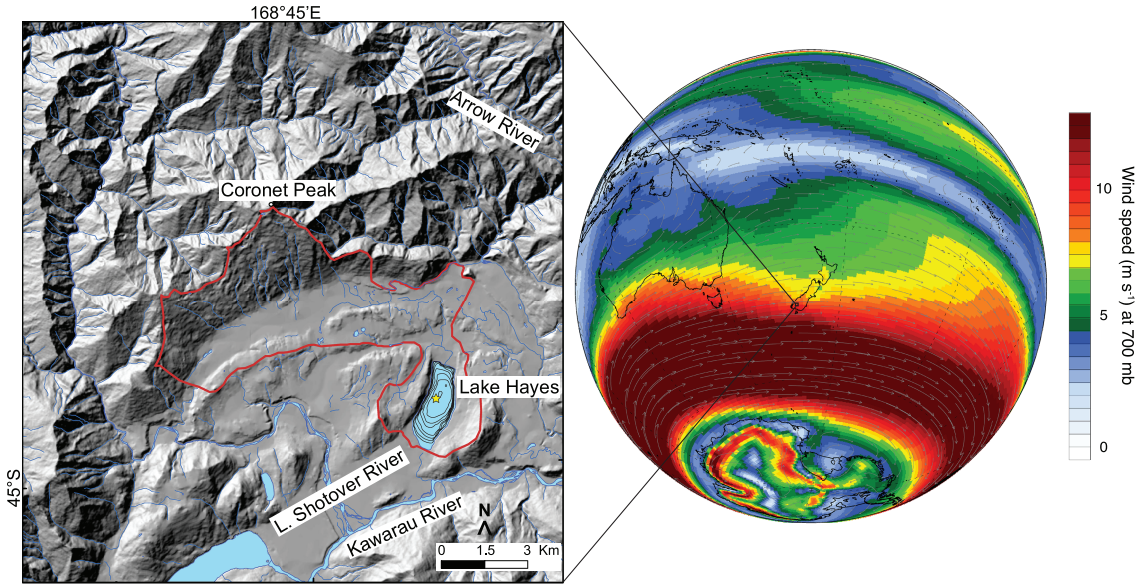

Figure 1. (right) Annual mean wind speeds at 700 hPa from ERA-Interim reanalysis data for 1979–2013. Map generated at cci-reanalyzer.org. (inset) Lake Hayes region and watershed (red outline). Black lines within the lake denote 2-m bathmetry contours (Jolly, 1968). Yellow star denotes core location.

increased precipitation (affecting the hydrologic balance) and/or a greater proportion of high-latitude moisture would lead to a more negative δD_{lake} value.

We measured the hydrogen stable isotopic composition (δD) of the *n*-alkane C_{23}. *n*-Alkanes of this chain length are thought to be primarily produced by nonemergent aquatic macrophytes (Ficken et al., 2000;

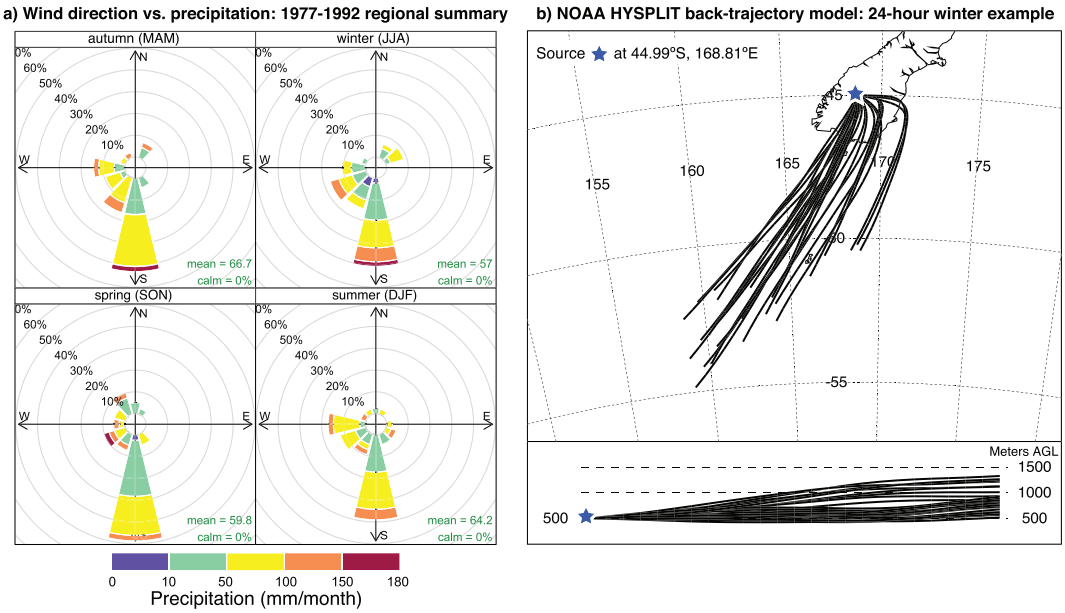

Figure 2. (a) Precipitation and wind direction data from Queenstown weather station collected in 1977–1992. Size of paddles corresponds to relative occurrence of precipitation events of a given amount. Direction of paddles corresponds to direction of wind gusts associated with precipitation events. Each quadrant represents seasonal averages for the sampling years. Note increased frequency of high-volume events during autumn/winter. Plot generated using the "openair" software package in R. (b) Example winter back trajectory plot from the National Oceanic and Atmospheric Administration Hysplit model, representing potential air and moisture pathways to Lake Hayes. Model generated for one 24-hr period in July 2014 to demonstrate common winter storm pathways from the Southern Ocean. Model generated at ready.arl.noaa.gov/HYSPLIT.php.

Sachse et al., 2004), meaning their primary source of hydrogen for compound synthesis is lake water and they are not subject to transpiration losses.

In open hydrological systems that have a relatively short residence time, lake water δD primarily reflects the isotopic composition of rainfall, which on the New Zealand South Island is influenced by temperature and changes in moisture source (Ummenhofer & England, 2007). However, if lake level drops below the outlet, the lake would become hydrologically closed and the primary influence on the δD of lake water will be evaporation, the extent of which is controlled by relative humidity. Similar controls have been postulated in more arid regions (e.g., the Tibetan Plateau), where aquatic macrophyte δD (from C23 *n*-alkanes) becomes enriched as lake water evaporation increases (Aichner et al., 2010). While the climatic setting is different, annual precipitation rates, catchment size, and lake size are relatively similar between Lake Hayes and the Aichner et al. (2010) study at Koucha Lake; thus, drivers in D enrichment/depletion may be similar.

In Lake Hayes, we expect the δD_{C23} to be influenced by both lake level, whereby increased evaporation or reduced input would lead to isotopic enrichment of the heavy isotope (D) (Gat, 1996), and moisture source latitude. Modern observations confirm that these two influences work in tandem: increased precipitation and higher-latitude moisture are coupled (Ummenhofer & England, 2007), both leading to a more negative δD signature. Conversely, when the westerlies are weak over New Zealand, we expect precipitation and lake level to decrease, which would elevate the δD_{C23} via evaporation.

Modern Lake Hayes surface water has average δD of -71 ± 4‰, and its primary inlet has an an average δD of -84 ± 5‰, both based on five measurements across different seasons in 2013–2014. Precipitation δD measured at a nearby station (located in Queenstown, New Zealand) across seasons from 2007–2010 was -47 ± 18‰ (Frew, 2015).

2.3. Carbonate Production in Lake Hayes

At Lake Hayes, trends in the δD_{C23} record will reflect two possible drivers: changes in hydrologic balance, changes in source input isotopic composition, or both, making it hard to deconvolve the relative influence of each. We add an additional proxy (sedimentary Ca/Ti) that is tied to hydrologic balance but independent of source isotopic input to separate the two factors. Changing Ca concentration in sediments can also be a result of two processes: different terrigenous inputs (provenance changes) or aqueous production of carbonate (Meyers:2001wz). Carbonate production within the water column can occur as a result of several processes, including evaporation of lake water and escape of CO_2 (Ito, 2001).

To differentiate between in situ carbonate production and provenance changes, we present Ca counts normalized to Ti counts from the X-ray fluorescence (XRF) core scanner. Ti is exclusively detrital, and detrital Ca and Ti will likely covary (Lowemark et al., 2011). The stoichiometric balance for the basement rocks in the watershed would result in a Ca/Ti from ~1–2 (Wandres et al., 2005); thus, very high Ca/Ti values are associated with endogenic carbonates (Jones & Bowser, 1978). Based on the consistent provenance and far distance from aeolian inputs (e.g., Australia), we do not expect significant Ti input variations in the Lake Hayes record.

Modern Lake Hayes is slightly alkaline, with a pH of 8.07 ± 0.16 ($n = 24$), $[Ca^{2+}]$ of 600 ± 8 μmol/L, and a total alkalinity of $1{,}400 \pm 20$ μmol/L (Reid et al., 1999). These latter two values fall close to the global averages for fresh waters, measured by Berner and Berner (1987). Reid et al. (1999) found seasonal biologic cycling of $CaCO_3$ in Lake Hayes, where biogenically formed carbonate sinks from the epilimnion and undergoes dissolution in the hypolimnion.

3. Materials and Analytical Methods

3.1. Sample Collection

Sediment cores were collected in Lake Hayes in November 2015 using an Uwitec percussion piston corer from an anchored platform. A ~6-m core was collected near the lake depocenter at 32-m water depth, and another ~4-m core was collected several meters away with a 1-m offset to obtain a continuous stratigraphy devoid of core breaks. A gravity corer was used to collect meter-long sediment cores containing the sediment-water interface. Cores were stored in a cool, dark place until being transported back to the University of Otago for refrigerated storage and analysis.

3.2. Sample Preparation

Physical properties of the whole sediment cores, including magnetic susceptibility, gamma density, and *P* wave velocity, were measured at the University of Otago using a Geotek Multi-Sensor Core Logger (2.6). After whole core scans, cores were split and the archive half was measured by Multi-Sensor Core Logger for point source magnetic susceptibility and high-resolution line scan imaging. Visual logs of sediment cores were also recorded to note significant color, texture, and lithological changes. We created a composite stratigraphy of undisturbed sediment from the percussion piston cores and the gravity core using CT images and physical properties data.

3.3. Lipid Extraction

Approximately 2–10 g of dry, homogenized sediment was weighed into Teflon containers, and 15 ml of a 9:1 mixture of dichloromethane and methanol was added to all samples. Samples were then placed in a CEM Microwave Accelerated Reaction System (MARS 5) for total lipid extraction. Collected solvent was vacuum filtered to remove all sediment from the total lipid extract and then treated with acid-cleaned copper filings to remove elemental sulfur. Next, the total lipid extracts were separated into different polarity fractions using solid-phase extraction. Approximately 0.5 g of packing material (Phenomenex Sepra™NH2) was packed into precombusted glass columns and washed with solvent. Samples were loaded onto columns, and the hydrocarbon fraction was eluted using 4 ml hexane. Hydrocarbon fractions were next eluted through Discovery® Ag-Ion solid phase extraction columns (750 mg, Supelco) to separate saturated from unsaturated compounds. The saturated fraction was eluted with 4 ml hexane.

3.4. *n*-Alkane Measurement by GC-MS/FID and GC-IRMS

To identify and quantify compounds, we measured saturated hydrocarbon fractions containing the *n*-alkanes on a ThermoScientific TraceGC equipped with a DB-5 ms column and a Programmable Temperature Vaporizing (PTV) injector, located in the Sessions Lab at Caltech. From the gas chromatography (GC), samples were split between a ThermoScientific TraceDSQ mass spectrometer and a flame ionization detector (FID). The GC oven was held at 100 °C for 1 min, ramped to 320° at 10°/min, and held at 320° for 10 min. Compounds were identified by comparison of mass spectra with library data. Abundances were calculated by comparing FID peak areas of compounds of interest with an internal standard (palmitic acid isobutyl ester) that was added prior to analysis.

Hydrogen isotope ratios of *n*-alkanes were measured on a ThermoScientific TraceGC coupled to a Delta $^{+}$XP with a pyrolysis interface operated at 1430 °C. Peaks were identified based on relative heights and elution times measured on the gas chromatography-mass spectrometry (GC-MS). The GC oven was operated under similar conditions as the GC-MS. To monitor machine performance, a CH_4 reference gas ($\delta D = -151.9‰$) was measured during sample runs, including before, after, and between sample peaks of interest. Repeat measurements of the palmitic acid isobutyl ester internal standard yielded an average δD of $-200.8 \pm 3.0‰$ ($n = 47$). All δD values are reported as permil deviations from the Vienna Standard Mean Ocean Water (VSMOW) standard.

The H_3^+ factor correction was performed before each batch run using an H_2 reference gas with known isotopic composition, following the method of Sessions et al. (2001). Over the course of all runs, the H_3^+ factor was 2.13 ± 0.07 ppm/mV. This correction and other data processing were performed in Isodat v2.5 software.

Carbon isotope ratios of *n*-alkanes were measured on a ThermoScientific TraceGC equipped with a Rxi®-5 ms (30 m × 0.25 mm, film thickness 0.25 mm) and a PTV injector at the Feakins IRMS (Isotope Ratio Mass Spectrometry) lab at the University of Southern California. The TraceGC is connected via GC Isolink with a combustion furnace at 1000 °C to a Delta V+ IRMS. Linearity of CO_2 measurements were measured daily (1 s, 0.05‰). Sample peaks were bracketed by reference peaks, two of which were used for standardization, between sample and standard, using a mixture of 15 *n*-alkanes (C_{16} to C_{30}) with $\delta^{13}C$ values ranging from −33.3 to −26.2‰ (A3 mix; supplied by A. Schimmelmann, Indiana University, USA) to normalize to the Vienna PeeDee Belemnite-Li SVEC (VPDB-LSVEC) carbon isotopic scale. The root-mean-square error of the external standards was better than 0.2‰.

3.5. Ice Volume Correction for δD

Measured δD values were corrected for ice volume changes following the approach in Tierney et al. (2011). This correction accounts for an 8‰ D-enrichment in the Last Glacial Maximum global ocean relative to

Table 1
Depth in Core and Measured Radiocarbon Age of Picked Macrofossil Samples From Lake Hayes

Composite depth (cm below lake floor)	^{14}C age	±	AMS Lab	Lab ID
62.5	885	35	CAMS	175191
127.5	3,270	45	CAMS	175192
151.5	3,750	30	CAMS	175193
198	3,985	24	Rafter	40868/1
241.5	4,710	60	CAMS	175135
269.5	6,909	32	Rafter	40868/2
290.5	8,615	40	CAMS	175137
346	9,718	42	Rafter	40868/4
393	11,020	160	CAMS	175195
468.5	12,561	57	Rafter	40868/5

Note. Samples were measured at two labs, the Center for Accelerator Mass Spectrometry (CAMS) and the Rafter Radiocarbon Laboratory run by GNS Science (Rafter).

today (Schrag et al., 1996; Shackleton, 2000), assuming no deuterium excess (Vimeux et al., 2001). The timing of the transition from a D-enriched ocean to modern values is scaled to the stacked benthic foraminiferal δ^{18}O record of Lisiecki and Raymo (2005).

3.6. Elemental Analysis by Scanning XRF

U-channels of sediment cores were measured on the Itrax XRF scanner (Cox Analytical Systems) at Lamont-Doherty Earth Observatory of Columbia University. Samples were analyzed with a molybdenum X-ray tube at 2-mm resolution, 4-s integration time, 30 kV and 55 mA. While a suite of elements were analyzed, we present calcium (Ca) relative concentrations normalized to titanium (Ti), a lithophilic element that is effectively measured by XRF and has been suggested as a good normalizer for Ca specifically (Hennekam & de Lange, 2012).

3.7. Radiocarbon Analysis and Age Model Generation

To determine the age of the sediments, terrestrial macrofossils and charcoal fragments were analyzed for radiocarbon content. Samples were pretreated at the University of Otago ^{14}C Preparation Lab using acid-alkali-acid pretreatment. Four samples were measured by accelerator mass spectrometry (AMS) at the Rafter Radiocarbon Facility at GNS Science New Zealand. Six additional samples were measured by AMS at the Center for Accelerator Mass Spectrometry at Lawrence Livermore National Laboratory. In addition, Queets-A wood fragments (expected age >80 ka) were pretreated and measured along with samples as procedural blanks.

Radiocarbon results (Table 1) were calibrated using the SHCal13 data set specific to the SH (Hogg et al., 2013). An age-depth model (Figure 3) was generated using the Bacon software (version 2.2) (Blaauw & Christen, 2011) developed for the R statistical platform, which utilizes a Bayesian statistical approach.

4. Results and Discussion

4.1. Age Model

The Lake Hayes sediment core spans from modern sediments to a calibrated weighted mean age of 17,543 cal yr BP, with all ages in stratigraphic order. The average accumulation rate over the entire core is ~0.3 mm/yr, but this increases slightly to ~0.4 mm/yr during the time period relevant to this study (~17.5–9 ka). The average 2σ range for calibrated ages is 334 years.

4.2. Discussion

4.2.1. Heinrich Stadial 1 (Base of Record to 14.7 ka) and the ACR (14.7–13.0 ka)

From the base of the record at ~17 ka to the end of the ACR, δD_{C23} undergoes a 35‰ depletion, which would suggest increased precipitation and/or a more southerly sourced moisture. The Ca/Ti record remains at stoichiometric balance (<2.0), which supports a wetter period but cannot discern potential changes in moisture source. During the ACR, there is a peak in zonal wind speed seen in the CCSM3 TraCE-21 ka coupled ocean-atmosphere general circulation model (He, 2011), simulated at 750 hPa at 46°S (Figure 4). Based on the modern linkage between moisture source, wind speed, and storm intensity (section 2.1 and Figure 2), the modelled wind speed peak is likely linked to both increased precipitation and southerly storm tracks.

Unlike C23, long-chain *n*-alkanes (e.g., C29 and C31) are considered primarily terrestrial, and their δD signatures reflect precipitation δD in temperate ecosystems (Sachse et al., 2006; Tipple & Pagani, 2013). Both δD_{C23} and $\delta D_{long\text{-}chain}$ should register shifts in precipitation source, yet δD_{C23} is likely to be more sensitive to precipitation volume and overall moisture balance, particularly in a small lake like Lake Hayes. From the base of the record to ~15 ka, the $\delta D_{long\text{-}chain}$ decreases by 15–20‰ (Figure 4), supporting an increase in southerly sourced moisture. However, the $\delta D_{long\text{-}chain}$ decouples from δD_{C23} during the ACR—while the latter continues to decrease to a minimum of 207‰, $\delta D_{long\text{-}chain}$ undergoes a slight increase and then remains fairly constant for the rest of the record. If $\delta D_{long\text{-}chain}$ reflects incoming precipitation δD, then the ACR at Lake Hayes is marked by high moisture balance but not an increase in southerly sourced moisture, as in Heinrich Stadial 1. To ensure that the decoupling of the two δD records is not driven by floral assemblage

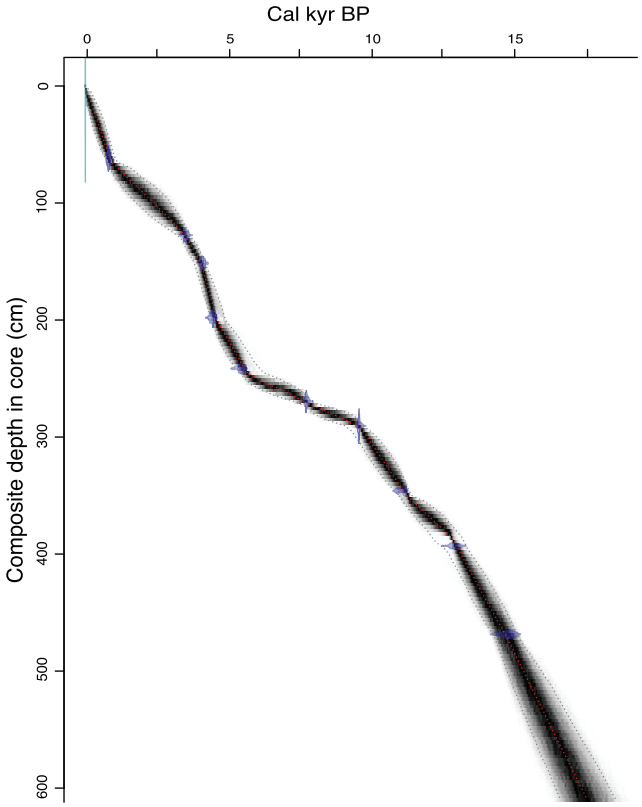

Figure 3. Age-depth model for Lake Hayes composite core (generated by Bacon 2.2 program in the R software platform). Calibrated using SHCal13. Blue shapes represent calibrated ^{14}C dates; gray lines represent possible age-depth relationships, with the red stippled line representing the best fit and the outer gray stippled line representing the 95% confidence intervals.

changes, we measured compound-specific $\delta^{13}C$ on long-chain *n*-alkanes. During the deglaciation, $\delta^{13}C_{long\text{-}chain}$ records change by <2‰, suggesting minor shifts in terrestrial vegetation types (see supporting information) (Chikaraishi & Naraoka, 2007).

4.2.2. The Younger Dryas (12.9–11.6 ka)

The two measures of paleohydrology in Lake Hayes, Ca/Ti and δD_{C23}, allow us to deconvolve the relative influences of source isotopic input and moisture balance. Ca/Ti responds to moisture balance alone; therefore, the large peak in Ca/Ti from 12.9–11.9 ka suggests a period of enhanced evaporation and possible lake closure. Sediments deposited at this time consist of ≥30% carbonate by weight, indicating carbonate precipitation far exceeds detrital inputs. This interval coincides with a zonal wind speed minimum in the TraCE-21 ka model, likely linked to less local precipitation and therefore a more negative moisture balance.

Unfortunately, the high concentration of carbonate during this interval corresponds to a dilution of organic matter; therefore, ability to measure δD_{C23} was restricted to a single sample with adequate concentration, which yielded a δD_{C23} of −200‰, similar to values from the ACR. Comparison with the Ca/Ti record rules out the possibility of increased precipitation/moisture balance, and comparison with the $\delta D_{long\text{-}chain}$ suggests no change in the source latitude of incoming precipitation. There appears to be a disconnect between the evaporative conditions indicated by the Ca/Ti, and no D-enrichment in the δD_{C23} record. A possible cause of the negative δD_{C23} could be contribution of high-altitude glacial meltwater. Kaplan et al. (2010) showed significant glacier retreat of mountain glaciers in New Zealand during the YD, and the contribution of this water would affect δD_{C23} but not $\delta D_{long\text{-}chain}$, as is observed.

The input of meltwater could also help explain the high Ca/Ti values during this time. Though the chemistry of the meltwater is unknown, modern studies of glacial meltwater chemistry from silicate bedrock environments show high concentrations of dissolved Ca^{2+} (Hosein et al., 2004; Li et al., 2019; West et al., 2002). If Lake Hayes was closed during the YD, pH would increase, and the combination of this with alkalinity input from glacial meltwater would drive endogenic carbonate precipitation.

4.2.3. The Early Holocene (11.6 ka to End of Record)

At the end of the YD and the beginning of the Holocene, δD_{C23} undergoes a positive shift of ~60‰. Modelled zonal wind speeds remain low (Figure 4). The δD_{C23} shift cannot be solely explained by a shift to more northerly precipitation, as there is little variation in the $\delta D_{long\text{-}chain}$ record from the YD through the early Holocene. It is difficult to quantify the possible drivers of an isotopic shift this large in Lake Hayes, in part because of the influence of evaporation on apparent enrichment factor (ε) between precipitation and mid-chain *n*-alkanes, as measured by Aichner et al. (2010). That study found that a decrease in precipitation by ~0.7 m/yr, over a similarly sized lake (Lake Koucha volume is ~6.2×10^7 m^3 compared to Lake Hayes at 4.7×10^7 m^3), could decrease ε by ~20‰ in aquatic macrophyte δD_{C23}.

Thus, it is likely that the early Holocene was marked by drier conditions leading to evaporative enrichment of D in Lake Hayes. During this interval, Ca/Ti falls back to detrital values, but glacial meltwater input also likely stopped after ~11.5 ka (Kaplan et al., 2010), thereby reducing alkalinity input into the lake that would facilitate endogenic carbonate production. Other regional evidence is consistent with drying and/or warming, such as continued glacial retreat (Putnam et al., 2012; Schaefer et al., 2009), low lake levels (Anderson et al., 2018), and establishment of temperate podocarp forests (McGlone et al., 2004).

4.2.4. The Lake Hayes Record in a Global Context

Though the Lake Hayes record provides insight into New Zealand's deglacial climate, hemispheric and global perspectives are necessary to explore forcing mechanisms. Deglacial changes in precipitation and

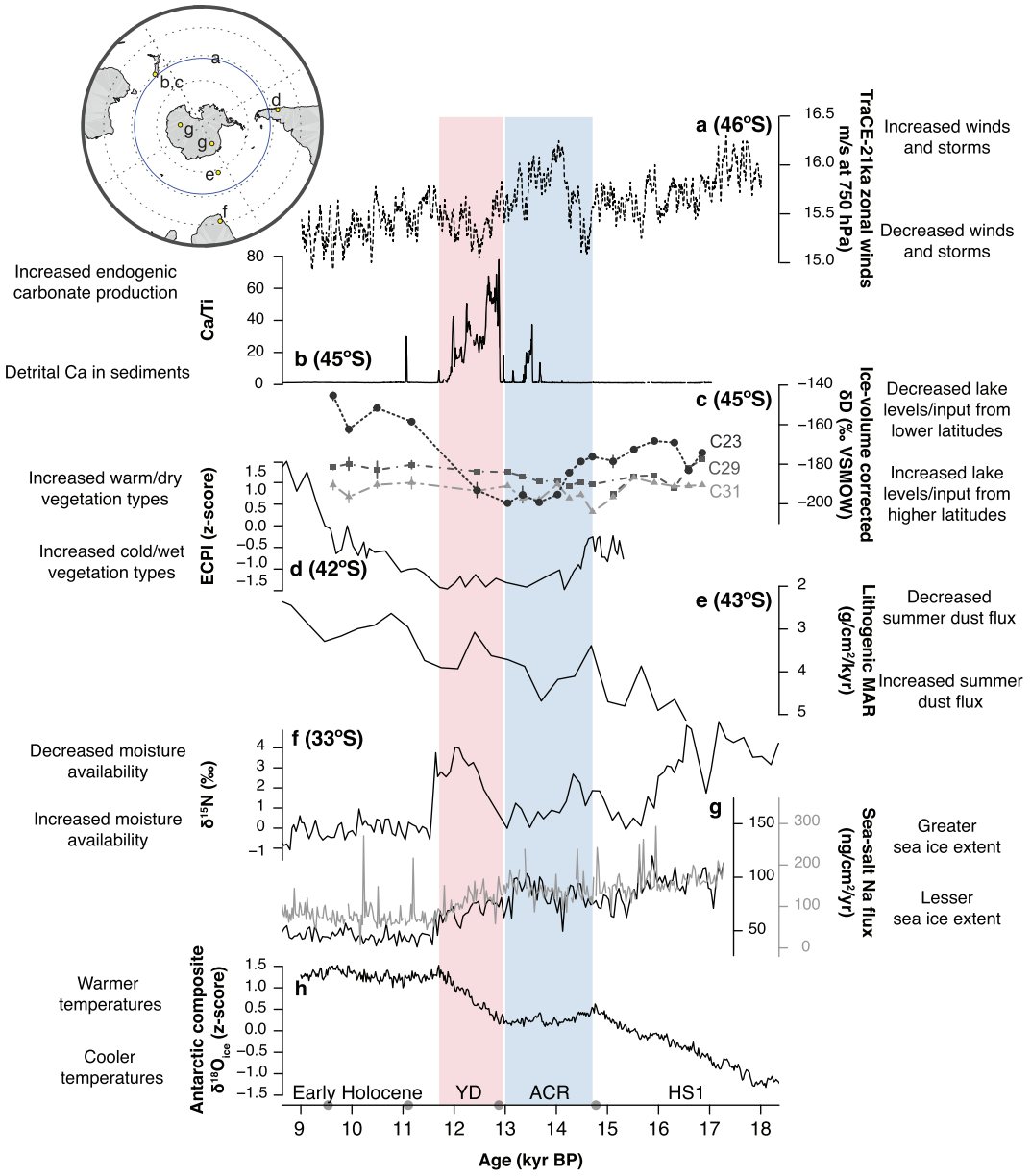

Figure 4. Southern Hemisphere deglacial climate model and records. (a) Zonal wind speeds at 750 hPa for 46°S from the TraCE-21 ka coupled atmosphere-ocean general circulation model (He, 2011). (b) Ca/Ti and (c) δD from Lake Hayes. Vertical bars represent 1 SD from replicate runs where possible. (d) *Eucryphia cordifolia* + *Caldcluvia paniculata* to Podocarpaceae (*Podocarpus nubigena* + *Saxegothaea conspicua*) index (ECPI) from Lago El Salto, Chile (Moreno & Videla, 2016). (e) Dust flux record from ODP site 1090 (Martínez-Garcia et al., 2014). (f) Hyrax midden $\delta^{15}N$ record from De Rif, South Africa (Chase et al., 2010; Chase et al., 2015). (g) Sea-salt Na flux, a proxy for sea ice extent, from EPICA Dome C (black) and EPICA Dronning Maud Land (gray) (Fischer et al., 2007; Wolff et al., 2006). (h) Composite Antarctic ice core $\delta^{18}O$ (Pedro et al., 2011). Inset map at top left shows locations of each record, as well as the latitudinal band represented by the TraCE-21 ka model. HS1: Heinrich Stadial 1. ACR: Antarctic Cold Reversal, denoted by blue bar. YD: Younger Dryas, denoted by red bar. Gray circles on *x* axis represent ages of ^{14}C samples.

temperature have been observed at other SH sites (Chase et al., 2010; Moreno & Videla, 2016; Pedro et al., 2016), but the duration and extent of millennial-scale shifts requires further exploration. Here we compare the Lake Hayes record to three other midlatitude sites (see Figure 4 inset for location) (Chase et al., 2015; Martínez-Garcia et al., 2011; Moreno & Videla, 2016), as well as Antarctic reconstructions of temperature and sea ice extent (Pedro et al., 2011; Röthlisberger et al., 2002; Wolff et al., 2006). The

midlatitude sites record wind intensity or westerly driven precipitation, making them suitable sites for comparison with Lake Hayes.

In South America, the Lago El Salto ECPI paleovegetation index (ratio of *Eucryphia cordifolia* + *Caldcluvia paniculata* to Podocarpaceae spp.) provides a proxy for hydrologic balance in the lowlands of the Chilean Lake District at 42°S. High (low) values indicate warm/dry (cold/wet) vegetation types (Moreno & Videla, 2016). In the South Atlantic, lithogenic mass accumulation rates increase at Ocean Drilling Program (ODP) site 1090 when summer dust flux is higher, linked to increased westerly wind strength (Lamy et al., 2015). At the nearby South African De Rif midden site, higher $\delta^{15}N$ values correspond to decreased water availability associated with a reduction in winter rainfall (Chase et al., 2015; Chase, Meadows, et al., 2010).

During the ACR, the four midlatitude sites compared here show a coherent shift toward increased windiness and/or rainfall (Figure 4). However, the duration of these shifts varies by site, and some cases, rebounds to drier/less windy conditions by the end of the climate anomaly. In a synthesis study of ACR records in the SH, Pedro et al. (2016) did not observe consistent precipitation anomalies in the midlatitudes when comparing mean values from the ACR interval to the 50 years before the ACR onset. Lake Hayes, which represents the highest latitude terrestrial site of the four, undergoes a shift of ~30‰ throughout the ACR. Associated with potential precipitation changes, New Zealand mean annual temperatures may have decreased by 1.8–3.2 °C (Doughty et al., 2013; Kaplan et al., 2010; Kaplan et al., 2013; Pedro et al., 2016). The other three sites show precipitation and/or wind maxima either during the ACR (ODP 1090) or at the ACR-YD transition (Lago El Salto and De Rif). While these proxies cannot quantitatively reconstruct changes in wind or precipitation, they do support the notion that all or part of the ACR was wetter and/or windier in the southern midlatitudes.

After the ACR, each site stabilizes or becomes drier to differing degrees. Lake Hayes undergoes a 60‰ positive shift in the δD_{C23} record from the YD to early Holocene, as well as a large increase in endogenic carbonate production during the YD caused by reduced lake water volume and likely topographic closure of the lake basin. Temperature reconstructions using reconstructed former ice margins suggest a shift of +3.6 °C between 13 and 11.8 ka (Kaplan et al., 2010), which could account for a hydrogen isotopic shift of up to 20‰ by using the Dansgaard (1964) equation ($\delta D = 5.6 * \text{mean annual air temperature} - 100‰$) to convert temperature to δD. A similarly sharp trajectory is seen at De Rif, where a shift to decreased moisture availability occurs within ~700 yr (Figure 4). While ODP 1090 reaches a dust flux minimum after an ACR maximum, values increase again throughout the YD. The Lago El Salto ECPI index shifts to a stable mode of warm/dry vegetation, which the authors interpret to persist through the early Holocene (Moreno et al., 2012; Moreno & Videla, 2016). In fact, the three sites above 40°S all continue a drying trend from the YD to the early Holocene (Figure 4).

The only site to experience an abrupt hydrologic shift is De Rif, which very rapidly shifts to a period of increased water availability at ~11.7 ka (Chase, Quick, et al., 2010). The authors suggest an increasing influence of the South Atlantic Anticyclone system on SW Africa, linked to changing conditions in the North Atlantic. Thus, this site potentially responds to climatic forcings from both hemispheres, especially during the millennial-scale deglacial climate anomalies. In the early Holocene, De Rif gets wetter while the higher-latitude sites discussed here continue in a drier state for several millennia. Based on this divergence, it appears that northern climatic influence overpowers changes happening in the southern midlatitudes at De Rif.

4.2.5. Potential Mechanisms to Explain Observed Climate Change

Millennial-scale climate anomalies during the last deglaciation have been documented in both the NH and SH, suggesting a global climate link. Heat and energy shift between the hemispheres, through both oceanic and atmospheric mediation (Barker et al., 2009; McGee et al., 2018; Pedro et al., 2016; Wunsch, 2006), which could provide a vehicle to connect the respective climates of each hemisphere.

In the deglacial ocean, large changes in North Atlantic freshwater inputs severely altered the pace and structure of the Atlantic meridional overturning circulation (Barker et al., 2010; McManus et al., 2004). Proxy reconstructions and model simulations point to a termination in freshwater discharge as the cause of BA warming in the NH (Clark et al., 2002; Liu et al., 2009; Peterson et al., 2000), which coincides with the ACR chronozone in the SH. As the Atlantic meridional overturning circulation strengthened in response, ocean heat transport in the SH underwent northward anomalies (Pedro et al., 2016), leading to observed

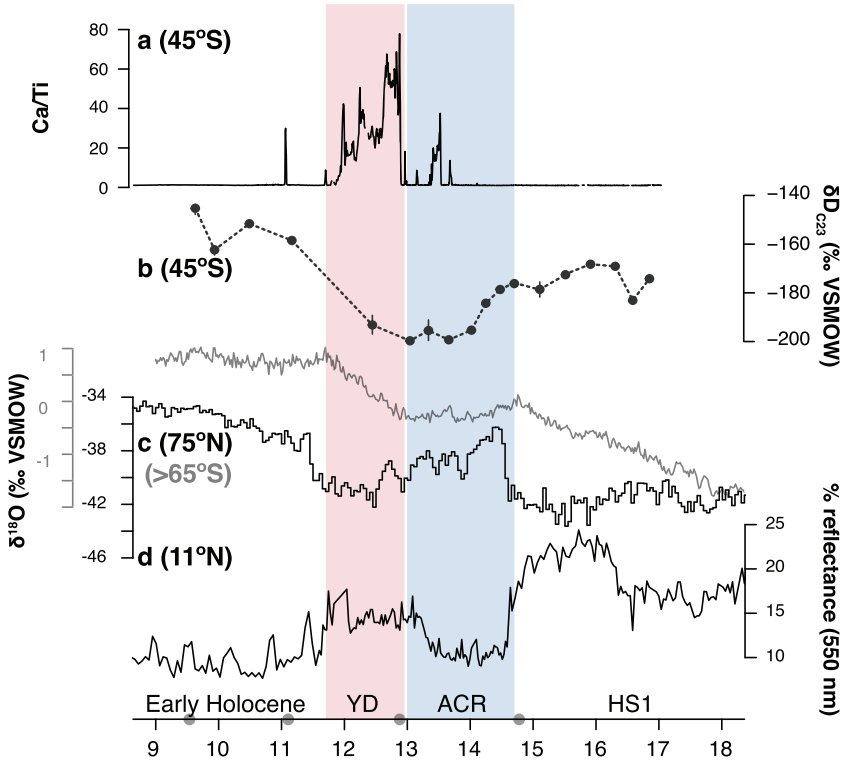

Figure 5. Comparison between Lake Hayes and Northern Hemisphere trends. (a and b) As in Figure 4. (c) Black: 50-year mean $\delta^{18}O$ measured in the North Greenland Ice Core Project (NGRIP) ice core (NGRIP Members, 2004). Gray: Antarctic composite ice core $\delta^{18}O$ *z* scores (Pedro et al., 2011). D, Color reflectance record from ODP site 1002 in the anoxic Cariaco basin (Peterson et al., 2000). Lower reflectance reflects increased organic productivity associated with warm interstadials and a northward ITCZ, whereas increased reflectance is a result of sediment deposited during cold stadials when the ITCZ shifts south.

cooling in the high-latitude SH. The trends in both hemispheres changed at the onset of the YD (~13.0 ka), almost simultaneously (Pedro et al., 2011). Although NH signals can be rapidly transmitted via the ocean to the SH by internal ocean waves (Masuda et al., 2010; Stocker & Johnsen, 2003), the near simultaneous onset of the deglacial climate anomalies suggests a strong role for atmospheric teleconnections.

One major atmospheric system that levies major influence on the midlatitude winds and precipitation is the Intertropical Convergence Zone, or ITCZ (Ceppi et al., 2013; Chiang et al., 2014). As the ITCZ shifts north (south), the cross-equatorial Hadley cell and associated subtropical jet strengthen (McGee et al., 2018); as a response, the midlatitude eddy-driven jet shifts toward the subtropical jet, or north (south) like the ITCZ (Ceppi et al., 2013). In short, through a series of atmospheric linkages, the ITCZ and midlatitude winds often move in tandem. Thus, mechanisms that drive shifts in the ITCZ may also drive changes in the westerlies. During the deglaciation, proxies measured in the Cariaco basin reconstruct ITCZ shifts during the ACR/BA and YD (Figure 5). When the NH warms and SH cools, as during the ACR, the ITCZ shifts toward the warmer hemisphere, recorded by color reflectance in Cariaco Basin sediments (Peterson et al., 2000). When the interhemispheric temperature gradient flips after 13 ka, the ITCZ migrates to the south.

Previous modeling studies have investigated different mechanisms that may cause ITCZ fluctuations, particularly opposite extratropical temperature trends in the NH and SH (Broccoli et al., 2006) and high-latitude ice cover changes (Chiang & Bitz, 2005). Interestingly, both forcing mechanisms cause the cooler or ice-growing hemisphere to become drier throughout, which conflicts with evidence from Lake Hayes and other midlatitude sites for increased precipitation during the ACR and decreased precipitation during the YD (Figure 4). It is possible that the midlatitudes do not reflect the hemispheric averages due to intensification and/or migration of westerly storm tracks associated with ITCZ shifts. When the ITCZ shifts toward the warmer hemisphere, as in the ACR, the core of the westerlies may also shift north, as is captured in the TraCE-21 ka model at 46°S (Figure 4). Conversely, during the YD, the westerlies may shift south or weaken in

tandem with the ITCZ migration. This would be registered in midlatitude sites as a combination of cool and wet and dry and warm, which is consistent with the Lake Hayes and other midlatitude records discussed here.

5. Conclusions

Using two independent paleohydrology proxies measured in a Lake Hayes, New Zealand, sediment core, we record distinct shifts in regional moisture balance during the last deglaciation. In particular, a negative δD_{C23} excursion of ~35‰ during the ACR suggests increasing southerly precipitation, which is consistent with trends in other SH midlatitude sites (Chase et al., 2015; Lamy et al., 2015; Moreno & Videla, 2016) and model results, particularly in the Pacific and Indian Ocean sectors (He et al., 2013; Pedro et al., 2016). At the ACR-YD transition (~13.0 ka), endogenic carbonate production, interpreted through Ca/Ti, increases rapidly in Lake Hayes as a likely response to lower lake levels and an input of glacial meltwater. In the early Holocene, δD_{C23} shifts by 60‰, but $\delta D_{long\text{-}chain}$ does not, suggesting drier conditions but not a shift in precipitation source. Again, similar drying patterns are seen elsewhere in the midlatitude SH. After the onset of the Holocene, the lowest latitude site (De Rif, 33°S) undergoes a rapid transition to increased moisture balance due to increasing NH influence (Chase et al., 2015). We find the New Zealand record to be consistent with other interpretations that the limit of NH influence during the deglaciation falls between 41°S and 45°S.

When compared to lower latitude atmospheric belts, particularly the ITCZ, the midlatitude westerlies appear to move in tandem during the millennial-scale deglacial anomalies. However, the two decouple during the early Holocene, wherein the ITCZ shifts north but the westerlies remain in a more southern position or weaker overall. A possible mechanism to explain this change is the full retreat of SH sea ice around 11.7 ka, which would exert a stronger influence on the SH westerlies than the ITCZ, which is more likely to respond to North Atlantic forcing (Broccoli et al., 2006; Chiang & Bitz, 2005). Due to the paucity of paleohydrologic data from this region, this record contributes to our understanding of midlatitude dynamics during the last deglaciation. Furthermore, as future climate change looms, it is imperative that we understand feedbacks within the climate system from past reconstructions to better forecast an uncertain path.

Acknowledgments
The data underlying this work can be found in the NOAA World Data Service for Paleoclimatology database (https://www.ncdc.noaa.gov/paleo-search/study/28171). Funding for field work was provided by a University of Otago Research Grant to C. M. M. J. L. H. was supported by the California Alliance for Graduate Education and The Professoriate (AGEP) and the Geological and Planetary Sciences Division at the California Institute of Technology. We thank Fenfang Wu for lab support and Brent Pooley, Greer Gilmer, Christina Riesselman, Harris Anderson, and Steve Little for help during fieldwork. Additional thanks to the Feakins IRMS Lab at USC for support and use of facilities. Finally, we are very grateful to one anonymous reviewer, Associate Editor Jim Russell, and Editor-in-Chief Ellen Thomas for their thoughtful and constructive feedback, which greatly improved this paper.

References

Aichner, B., Herzschuh, U., Wilkes, H., Vieth, A., & Böhner, J. (2010). δD values of *n*-alkanes in Tibetan lake sediments and aquatic macrophytes—A surface sediment study and application to a 16 ka record from Lake Koucha. *Organic Geochemistry*, *41*(8), 779–790. https://doi.org/10.1016/j.orggeochem.2010.05.010

Anderson, H. J., Moy, C. M., Vandergoes, M. J., Nichols, J. E., Riesselman, C. R., & Van Hale, R. (2018). Southern Hemisphere westerly wind influence on southern New Zealand hydrology during the Lateglacial and Holocene. *Journal of Quaternary Science*, *33*(6), 689–701. https://doi.org/10.1002/jqs.3045

Anderson, R. F., & Carr, M. E. (2010). Uncorking the Southern Ocean's vintage CO_2. *Science*, *328*(5982), 1117–1118. https://doi.org/10.1126/science.1190765

Barker, S., Diz, P., Vautravers, M. J., Pike, J., Knorr, G., Hall, I. R., & Broecker, W. S. (2009). Interhemispheric Atlantic seesaw response during the last deglaciation. *Nature*, *457*(7233), 1097–1102. https://doi.org/10.1038/nature07770

Barker, S., Knorr, G., Vautravers, M. J., Diz, P., & Skinner, L. C. (2010). Extreme deepening of the Atlantic overturning circulation during deglaciation. *Nature Geoscience*, *3*(8), 567–571. https://doi.org/10.1038/ngeo921

Berner, E. K., & Berner, R. A. (1987). *Global water cycle: Geochemistry and environment*. Englewood Cliffs, New Jersey: Prentice-Hall.

Blaauw, M., & Christen, J. A. (2011). Flexible paleoclimate age-depth models using an autoregressive gamma process. *Bayesian Analysis*, *6*(3), 457–474.

Brauer, A., Haug, G. H., Dulski, P., Sigman, D. M., & Negendank, J. F. W. (2008). An abrupt wind shift in western Europe at the onset of the Younger Dryas cold period. *Nature Geoscience*, *1*(8), 520–523. https://doi.org/10.1038/ngeo263

Broccoli, A. J., Dahl, K. A., & Stouffer, R. J. (2006). Response of the ITCZ to Northern Hemisphere cooling. *GRL*, *33*(1), 1, n/a–4. https://doi.org/10.1029/2005gl024546

Broecker, W. S. (1998). Paleocean circulation during the last deglaciation: A bipolar seesaw? *Paleoceanography*, *13*(2), 119–121. https://doi.org/10.1029/97PA03707

Ceppi, P., Hwang, Y. T., Liu, X., Frierson, D. M. W., & Hartmann, D. L. (2013). The relationship between the ITCZ and the Southern Hemispheric eddy-driven jet. *Journal of Geophysical Research: Atmospheres*, *118*, 5136–5146. https://doi.org/10.1002/jgrd.50461

Chase, B. M., Boom, A., Carr, A. S., Carré, M., Chevalier, M., Meadows, M. E., et al. (2015). Evolving southwest African response to abrupt deglacial North Atlantic climate change events. *Quaternary Science Reviews*, *121*(C), 132–136. https://doi.org/10.1016/j.quascirev.2015.05.023

Chase, B. M., Meadows, M. E., Carr, A. S., & Reimer, P. J. (2010). Evidence for progressive Holocene aridification in southern Africa recorded in Namibian hyrax middens: Implications for African Monsoon dynamics and the "African humid period". *Quaternary Research*, *74*(1), 36–45. https://doi.org/10.1016/j.yqres.2010.04.006

Chase, B. M., Quick, L. J., Meadows, M. E., Scott, L., Thomas, D. S. G., & Reimer, P. J. (2010). Late glacial interhemispheric climate dynamics revealed in South African hyrax middens. *Geology*, *39*(1), 19–22. https://doi.org/10.1130/G31129.1

Chiang, J. C. H., & Bitz, C. M. (2005). Influence of high latitude ice cover on the marine Intertropical Convergence Zone. *Climate Dynamics*, *25*(5), 477–496. https://doi.org/10.1007/s00382-005-0040-5

Chiang, J. C. H., Lee, S. Y., Putnam, A. E., & Wang, X. (2014). South Pacific split jet, ITCZ shifts, and atmospheric north–south linkages during abrupt climate changes of the last glacial period. *Earth and Planetary Science Letters*, *406*(C), 233–246. https://doi.org/10.1016/j.epsl.2014.09.012

Chikaraishi, Y., & Naraoka, H. (2007). $\delta^{13}C$ and δD relationships among three *n*-alkyl compound classes (*n*-alkanoic acid, *n*-alkane and *n*-alkanol) of terrestrial higher plants. *Organic Geochemistry*, *38*(2), 198–215. https://doi.org/10.1016/j.orggeochem.2006.10.003

Clark, P. U., Pisias, N. G., Stocker, T. F., & Weaver, A. J. (2002). The role of the thermohaline circulation in abrupt climate change. *Nature*, *415*(6874), 863–869. https://doi.org/10.1038/415863a

Clark, P. U., Shakun, J. D., & Baker, P. A. (2012). Global climate evolution during the last deglaciation. *Proceedings of the National Academy of Sciences*, *109*(19), E1134–E1142. https://doi.org/10.1073/pnas.1116619109/-/DCSupplemental

Dansgaard, W. (1964). Stable isotopes in precipitation. *Tellus*, *16*, 436–468. https://doi.org/10.3402/tellusa.v16i4.8993

Denton, G. H., Anderson, R. F., Toggweiler, J. R., Edwards, R. L., Schaefer, J. M., & Putnam, A. E. (2010). The Last Glacial Termination. *Science*, *328*(5986), 1652–1656. https://doi.org/10.1126/science.1184119

Doughty, A. M., Anderson, B. M., Mackintosh, A. N., Kaplan, M. R., Vandergoes, M. J., Barrell, D. J. A., et al. (2013). Evaluation of Lateglacial temperatures in the Southern Alps of New Zealand based on glacier modelling at Irishman Stream, Ben Ohau Range. *Quaternary Science Reviews*, *74*, 160–169. https://doi.org/10.1016/j.quascirev.2012.09.013

Ficken, K. J., Li, B., Swain, D. L., & Eglinton, G. (2000). An *n*-alkane proxy for the sedimentary input of submerged/floating freshwater aquatic macrophytes. *Organic Geochemistry*, *31*(7-8), 745–749. https://doi.org/10.1016/S0146-6380(00)00081-4

Fischer, H., Fundel, F., Ruth, U., Twarloh, B., Wegner, A., Udisti, R., et al. (2007). Reconstruction of millennial changes in dust emission, transport and regional sea ice coverage using the deep EPICA ice cores from the Atlantic and Indian Ocean sector of Antarctica. *Earth and Planetary Science Letters*, *260*, 340–354. https://doi.org/10.1016/j.epsl.2007.06.014

Frew, R. (2015). *A stable isotope rainfall map for the protection of NZ's biological and environmental resources*. Prepared For: CDRP Isotopes in Precipitation Project Steering Group, MAF Biosecurity and Department of Conservation. https://doi.org/10.13140/RG.2.1.2971.6967

Garreaud, R., Lopez, P., Minvielle, M., & Rojas, M. (2013). Large-scale control on the Patagonian climate. *Journal of Climate*, *26*(1), 215–230 . https://doi.org/10.1175/JCLI-D-12-00001.1

Gat, J. R. (1996). Oxygen and hydrogen isotopes in the hydrologic cycle. *Annual Review of Earth and Planetary Sciences*, *24*(1), 225–262. https://doi.org/10.1146/annurev.earth.24.1.225

He, F. (2011), Simulating transient climate evolution of the last deglaciation with CCSM3, 1–185 pp.

He, F., Shakun, J. D., Clark, P. U., Carlson, A. E., Liu, Z., Otto-Bliesner, B. L., & Kutzbach, J. E. (2013). Northern Hemisphere forcing of Southern Hemisphere climate during the last deglaciation. *Nature*, *494*(7435), 81–85. https://doi.org/10.1038/nature11822

Hennekam, R., & de Lange, G. (2012). X-ray fluorescence core scanning of wet marine sediments: Methods to improve quality and reproducibility of high-resolution paleoenvironmental records. *Limnology and Oceanography: Methods*, *10*(12), 991–1003. https://doi.org/10.4319/lom.2012.10.991

Hodell, D. A., Turchyn, A. V., Wiseman, C. J., Escobar, J., Curtis, J. H., Brenner, M., et al. (2012). Late glacial temperature and precipitation changes in the lowland neotropics by tandem measurement of $d^{18}O$ in biogenic carbonate and gypsum hydration water. *Geochimica et Cosmochimica Acta*, *77*(C), 352–368. https://doi.org/10.1016/j.gca.2011.11.026

Hogg, A. G., et al. (2013). SHCal13 Southern Hemisphere calibration, 0–50,000 cal yr BP. *Radiocarbon*, *55*(2), 1–15.

Hosein, R., Arn, K., Steinmann, P., Adatte, T., & Föllmi, K. B. (2004). Carbonate and silicate weathering in two presently glaciated, crystalline catchments in the Swiss Alps. *Geochimica et Cosmochimica Acta*, *68*(5), 1021–1033. https://doi.org/10.1016/S0016-7037(03)00445-9

IAEA/WMO (2016), Global network for isotopes in precipitation,

Ito, E. (2001). 13. Application of stable isotope techniques to inorganic and biogenic carbonates. In W. M. Last, & J. P. Smol (Eds.), *Tracking environmental change using lake sediments. Volume 2: Physical and geochemical methods, vol. 2* (pp. 351–370). Dordrecht, The Netherlands: Kluwer Academic Publishers.

Jolly, V. H. (1968). The comparative limnology of some New Zealand lakes. *New Zealand Journal of Marine and Freshwater Research*, *2*(2), 214–259. https://doi.org/10.1080/00288330.1968.9515236

Jones, B. F., & Bowser, C. J. (1978). The mineralogy and related chemistry of lake sediments. In *Lakes* (pp. 179–235). New York, NY: Springer New York. https://doi.org/10.1007/978-1-4757-1152-3_7

Kaplan, M. R., Schaefer, J. M., Denton, G. H., Barrell, D. J. A., Chinn, T. J. H., Putnam, A. E., et al. (2010). Glacier retreat in New Zealand during the Younger Dryas stadial. *Nature*, *467*(7312), 194–197. https://doi.org/10.1038/nature09313

Kaplan, M. R., Schaefer, J. M., Denton, G. H., Doughty, A. M., Barrell, D. J. A., Chinn, T. J. H., et al. (2013). The anatomy of long-term warming since 15 ka in New Zealand based on net glacier snowline rise. *Geology*, *41*(8), 887–890. https://doi.org/10.1130/G34288.1

Klinger, B. A., & Cruz, C. (2009). Decadal response of global circulation to Southern Ocean zonal wind stress perturbation. *Journal of Physical Oceanography*, *39*(8), 1888–1904. https://doi.org/10.1175/2009JPO4070.1

Lamy, F., Arz, H. W., Kilian, R., Lange, C. B., Lembke-Jene, L., Wengler, M., et al. (2015). Glacial reduction and millennial-scale variations in Drake Passage throughflow. *Proceedings of the National Academy of Sciences*, *112*(44), 13496–13501. https://doi.org/10.1073/pnas.1509203112

Li, X., Ding, Y., Liu, Q., Zhang, Y., Han, T., Jing, Z., et al. (2019). Intense chemical weathering at glacial meltwater-dominated Hailuogou Basin in the southeastern Tibetan Plateau. *Water*, *11*(6), 1209–1222. https://doi.org/10.3390/w11061209

Lisiecki, L. E., & Raymo, M. E. (2005). A Pliocene-Pleistocene stack of 57 globally distributed benthic $\delta^{18}O$ records. *Paleoceanography*, *20*, n/a–n/a, PA1003. https://doi.org/10.1029/2004PA001071

Liu, D., Wang, Y., Cheng, H., Kong, X., & Chen, S. (2013). Centennial-scale Asian monsoon variability during the mid-Younger Dryas from Qingtian Cave, central China. *Quaternary Research*, *80*(2), 199–206. https://doi.org/10.1016/j.yqres.2013.06.009

Liu, Z., Otto-Bliesner, B. L., He, F., Brady, E. C., Tomas, R., Clark, P. U., et al. (2009). Transient simulation of last deglaciation with a new mechanism for Bølling-Allerød warming. *Science*, *325*(5938), 310–314. https://doi.org/10.1126/science.1171041

Lowemark, L., Chen, H. F., Yang, T.-N., Earth, M. K., Yu, E.-F., Hsu, Y.-W., et al. (2011). Normalizing XRF-scanner data: A cautionary note on the interpretation of high-resolution records from organic-rich lakes. *Journal of Asian Earth Sciences*, *40*(6), 1250–1256. https://doi.org/10.1016/j.jseaes.2010.06.002

Martínez-Garcia, A., Rosell-Melé, A., Jaccard, S. L., Geibert, W., Sigman, D. M., & Haug, G. H. (2011). Southern Ocean dust–climate coupling over the past four million years. *Nature*, *476*(7360), 312–315. https://doi.org/10.1038/nature10310

Martínez-García, A., Sigman, D. M., Ren, H., Anderson, R. F., Straub, M., Hodell, D. A., Jaccard, S. L., et al. (2014). Iron fertilization of the Subantarctic Ocean during the last Ice Age. *Science*, *343*(6177), 1347–1350. https://doi.org/10.1126/science.1246848

Masuda, S., Awaji, T., Sugiura, N., Matthews, J. P., Toyoda, T., Kawai, Y., et al. (2010). Simulated rapid warming of abyssal North Pacific waters. *Science*, *329*(5989), 319–322. https://doi.org/10.1126/science.1188703

McGee, D., Moreno-Chamarro, E., Green, B., Marshall, J., Galbraith, E., & Bradtmiller, L. (2018). Hemispherically asymmetric trade wind changes as signatures of past ITCZ shifts. *Quaternary Science Reviews*, *180*, 214–228. https://doi.org/10.1016/j.quascirev.2017.11.020

McGlone, M. S., Turney, C., & Wilmshurst, J. M. (2004). Late-glacial and Holocene vegetation and climatic history of the Cass Basin, central South Island. *New Zealand, Quaternary Research*, *62*, 267–279.

McManus, J. F., François, R., Gherardi, J. M., Keigwin, L. D., & Brown-Leger, S. (2004). Collapse and rapid resumption of Atlantic meridional circulation linked to deglacial climate changes. *Nature*, *428*(6985), 834–837. https://doi.org/10.1038/nature02494

Moreno, P. I., & Videla, J. (2016). Centennial and millennial-scale hydroclimate changes in northwestern Patagonia since 16,000 yr BP. *Quaternary Science Reviews*, *149*, 326–337. https://doi.org/10.1016/j.quascirev.2016.08.008

Moreno, P. I., Villa-Martínez, R., Cárdenas, M. L., & Sagredo, E. A. (2012). Deglacial changes of the southern margin of the southern westerly winds revealed by terrestrial records from SW Patagonia (52S). *Quaternary Science Reviews*, *41*(C), 1–21. https://doi.org/10.1016/j.quascirev.2012.02.002

Otago Regional Council (2009). *Otago lakes' trophic status.* https://www.orc.govt.nz/media/6192/web-version-otago-lakes-trophic-status.pdf.

Pedro, J. B., Bostock, H. C., Bitz, C. M., & He, F. (2016). The spatial extent and dynamics of the Antarctic Cold Reversal. *Nature Geoscience*, *9*(1), 51–55. https://doi.org/10.1038/ngeo2580

Pedro, J. B., van Ommen, T. D., Rasmussen, S. O., Morgan, V. I., Chappellaz, J., Moy, A. D., et al. (2011). The last deglaciation: Timing the bipolar seesaw. *Climate of the Past Discussions*, *7*(1), 397–430. https://doi.org/10.5194/cpd-7-397-2011

Peterson, L. C., Haug, G. H., Hughen, K. A., & Röhl, U. (2000). Rapid changes in the hydrologic cycle of the tropical Atlantic during the last glacial. *Science*, *290*(5498), 1947–1951. https://doi.org/10.1126/science.290.5498.1947

Purdie, H., Bertler, N., Mackintosh, A., Baker, J., & Rhodes, R. (2010). Isotopic and elemental changes in winter snow accumulation on glaciers in the Southern Alps of New Zealand. *Journal of Climate*, *23*(18), 4737–4749. https://doi.org/10.1175/2010JCLI3701.1

Putnam, A. E., Schaefer, J. M., Denton, G. H., Barrell, D. J. A., Finkel, R. C., Andersen, B. G., et al. (2012). Regional climate control of glaciers in New Zealand and Europe during the pre-industrial Holocene. *Nature Geoscience*, *5*(9), 627–630. https://doi.org/10.1038/ngeo1548

Reid, M. R., Kim, J. P., & Hunter, K. A. (1999). Trace metal and major ion concentrations in Lakes Hayes and Manapouri. *Journal of the Royal Society of New Zealand*, *29*(3), 245–255. https://doi.org/10.1080/03014223.1999.9517595

Röthlisberger, R., Mulvaney, R., Wolff, E. W., Hutterli, M. A., Bigler, M., Sommer, S., & Jouzel, J. (2002). Dust and sea salt variability in central East Antarctica (Dome C) over the last 45 kyrs and its implications for southern high-latitude climate. *Geophysical Research Letters*, *29*(20), 1963. https://doi.org/10.1029/2002GL015186

Sachse, D., Radke, J., & Gleixner, G. (2004). Hydrogen isotope ratios of recent lacustrine sedimentary *n*-alkanes record modern climate variability. *Geochimica et Cosmochimica Acta*, *68*(23), 4877–4889. https://doi.org/10.1016/j.gca.2004.06.004

Sachse, D., Radke, J., & Gleixner, G. (2006). δD values of individual *n*-alkanes from terrestrial plants along a climatic gradient—Implications for the sedimentary biomarker record. *Organic Geochemistry*, *37*(4), 469–483. https://doi.org/10.1016/j.orggeochem.2005.12.003

Salinger, M. J., & Mullan, A. B. (2001). New Zealand climate: Temperature and precipitation variations and their links with atmospheric circulation 1930–1994. *International Journal of Climatology*, *19*(10), 1049–1071. https://doi.org/10.1002/(SICI)1097-0088(199908)19:10<1049::AID-JOC417>3.0.CO;2-Z

Schaefer, J. M., Denton, G. H., Kaplan, M., Putnam, A., Finkel, R. C., Barrell, D. J. A., et al. (2009). High-frequency Holocene glacier fluctuations in New Zealand differ from the northern signature. *Science*, *324*(5927), 622–625. https://doi.org/10.1126/science.1169312

Schrag, D. P., Hampt, G., & Murray, D. W. (1996). Pore fluid constraints on the temperature and oxygen isotopic composition of the glacial ocean. *Science*, *272*(5270), 1930–1932. https://doi.org/10.1126/science.272.5270.1930

Sessions, A. L., Burgoyne, T. W., & Hayes, J. M. (2001). Determination of the H_3 factor in hydrogen isotope ratio monitoring mass spectrometry. *Analytical Chemistry*, *73*(2), 200–207. https://doi.org/10.1021/ac000488m

Shackleton, N. J. (2000). The 100,000-year ice-age cycle identified and found to lag temperature, carbon dioxide, and orbital eccentricity. *Science*, *289*(5486), 1897–1902. https://doi.org/10.1126/science.289.5486.1897

Stocker, T. F., & Johnsen, S. J. (2003). A minimum thermodynamic model for the bipolar seesaw. *Paleoceanography*, *18*(4), n/a–n/a), 1087. https://doi.org/10.1029/2003PA000920

Tierney, J. E., Russell, J. M., Sinninghe Damsté, J. S., Huang, Y., & Verschuren, D. (2011). Late Quaternary behavior of the East African monsoon and the importance of the Congo Air Boundary. *Quaternary Science Reviews*, *30*(7-8), 798–807. https://doi.org/10.1016/j.quascirev.2011.01.017

Tipple, B. J., & Pagani, M. (2013). Environmental control on eastern broadleaf forest species' leaf wax distributions and D/H ratios. *Geochimica et Cosmochimica Acta*, *111*, 64–77. https://doi.org/10.1016/j.gca.2012.10.042

Toggweiler, J. R., Russell, J. L., & Carson, S. R. (2006). Midlatitude westerlies, atmospheric CO_2, and climate change during the ice ages. *Paleoceanography*, *21*, PA2005. https://doi.org/10.1029/2005PA001154

Ummenhofer, C. C., & England, M. H. (2007). Interannual extremes in New Zealand precipitation linked to modes of Southern Hemisphere climate variability. *Journal of Climate*, *20*(21), 5418–5440. https://doi.org/10.1175/2007JCLI1430.1

Vimeux, F., Masson, V., Delaygue, G., Jouzel, J., Petit, J. R., & Stievenard, M. (2001). A 420,000 year deuterium excess record from East Antarctica: Information on past changes in the origin of precipitation at Vostok. *Journal of Geophysical Research Atmospheres*, *106*(D23), 31863–31873. https://doi.org/10.1029/2001JD900076

Wandres, A. M., Bradshaw, J. D., & Ireland, T. (2005). The Paleozoic-Mesozoic recycling of the Rakaia Terrane, South Island, New Zealand: Sandstone clast and sandstone petrology, geochemistry, and geochronology. *New Zealand Journal of Geology and Geophysics*, *48*(2), 229–245. https://doi.org/10.1080/00288306.2005.9515112

West, A. J., Bickle, M. J., Collins, R., & Brasington, J. (2002). Small-catchment perspective on Himalayan weathering fluxes | Geology | GeoScienceWorld. *Geology*, *30*(4), 355–358. https://doi.org/10.1130/0091-7613(2002)030<0355:SCPOHW>2.0.CO;2

Wolff, E. W., Fischer, H., Fundel, F., Ruth, U., Twarloh, B., Littot, G. C., et al. (2006). Southern Ocean sea-ice extent, productivity and iron flux over the past eight glacial cycles. *Nature*, *440*(7083), 491–496. https://doi.org/10.1038/nature04614

Wunsch, C. (2006). Abrupt climate change: An alternative view. *Quaternary Research*, *65*(02), 191–203. https://doi.org/10.1016/j.yqres.2005.10.006